ADVANCED FUNCTIONAL MATERIALS
www.afm-journal.de

Hybrid of Iron Nitride and Nitrogen-Doped Graphene Aerogel as Synergistic Catalyst for Oxygen Reduction Reaction

*Han Yin, Chenzhen Zhang, Fei Liu, and Yanglong Hou**

It is extremely desirable but challenging to create highly active, stable, and low-cost catalysts towards oxygen reduction reaction to replace Pt-based catalysts in order to perform the commercialization of fuel cells. Here, a novel iron nitride/nitrogen doped-graphene aerogel hybrid, synthesized by a facile two-step hydrothermal process, in which iron phthalocyanine is uniformly dispersed and anchored on graphene surface with the assist of π–π stacking and oxygen-containing functional groups, is reported. As a result, there exist strong interactions between Fe_xN nanoparticles and graphene substrates, leading to a synergistic effect towards oxygen reduction reaction. It is worth noting that the onset potential and current density of the hybrid are significantly better and the charge transfer resistance is much lower than that of pure nitrogen-doped graphene aerogel, free Fe_xN and their physical mixtures. The hybrid also exhibits comparable catalytic activity as commercial Pt/C at the same catalyst loading, while its stability and resistance to methanol crossover are superior. Interestingly, it is found that, apart from the active nature of the hybrid, the large surface area and porosity are responsible for its excellent onset potential and the high density of Fe–N–C sties and small size of Fe_xN particles boost charge transfer rate.

1. Introduction

Fuel cells with their high energy and power density have been widely considered as green and efficient alternative energy sources. However, the sluggish oxygen reduction reaction (ORR) usually needs to be catalyzed by Pt-based electrocatalysts, which exhibit excellent catalytic activity, but suffer from prohibitive cost, susceptibility to methanol crossover and poor stability. These drawbacks remain the bottlenecks of the commercialization of fuel cells. Consequently, alternative ORR catalysts with high catalytic activity and selectivity, strong durability and low cost are extremely desired.

Doped carbon materials have been investigated as ORR catalysts in alkaline electrolytes.[1] Among them, doped graphene has attracted intensive interest due to its good catalytic activity, high electrical conductivity, large surface area and good chemical stability.[2] On the other hand, loading nonprecious metals,[3] metal oxides,[4] metal chalcogenides[5] or metal-N_4 structured macrocyclic compounds[6] onto carbonaceous supports has also been demonstrated to be effective in improving ORR catalytic activity. However, in order to achieve similar current density as Pt/C, the loading amount of catalysts were usually several times higher than that of Pt/C.[7] As a result, it brings a challenge for these materials to achieve excellent catalytic activity as well as strong durability.

Recently, three dimensional (3D) carbon networks emerged to be more effective in catalyzing ORR than their one dimensional or two dimensional counterparts due to their large surface area, rich macropores and multiplex electron transfer pathways.[8] Moreover, using graphene oxide (GO) as a precursor, the oxygen-containing functional groups on GO would facilitate the effective linking between graphene and nanoparticles, which may contribute to the synergistic effect.[9] All these characteristics allowed 3D graphene to be an ideal substrate for catalyst particles. Nevertheless, current 3D graphene frameworks based catalysts failed to reach comparative catalytic activity to that of Pt/C.[8a,10] As a result, further exploration of this new kind of substrate is highly anticipated.

In addition, it has been proposed that M–N–C (M = Fe and/or Co) structure could be the active sites of ORR catalysts.[11] Besides metal-N_4 macrocycles, composites of Fe or Fe-containing compounds and N-doped carbonaceous materials may be prospective candidates. Parvez et al. synthesized nitrogen-doped graphene (NG) decorated with Fe nanoparticles which showed enhanced ORR catalytic activity than metal-free NG.[12] Wang et al. reported a composite of Fe_2N/N-doped graphitic nanocarbons as ORR catalyst through an ion-exchanged route.[13] However, a gap still remains between these recently reported materials and Pt/C with respect to onset potential and mass activity, which might limit their future applications.

Based on this situation, it is highly desirable to propose a strategy to maximize the density of M–N–C active sites. The first way is to introduce a metal nitride into graphene substrate. Iron nitrides have been reported to be capable of forming active Fe–N–C sites on carbon.[14] FeN, a relatively new kind of iron nitride, has never been applied as ORR catalyst to the best of our knowledge, presumably because it is difficult to be synthesized. However, this phase is rich in nitrogen and is therefore likely to form Fe–N–C structures more effectively on graphene. Minimizing the particle size is another way which can greatly

H. Yin, C. Zhang, F. Liu, Prof. Y. Hou
Department of Materials Science and Engineering
College of Engineering, Peking University
Beijing 100871, China
E-mail: hou@pku.edu.cn

DOI: 10.1002/adfm.201303902

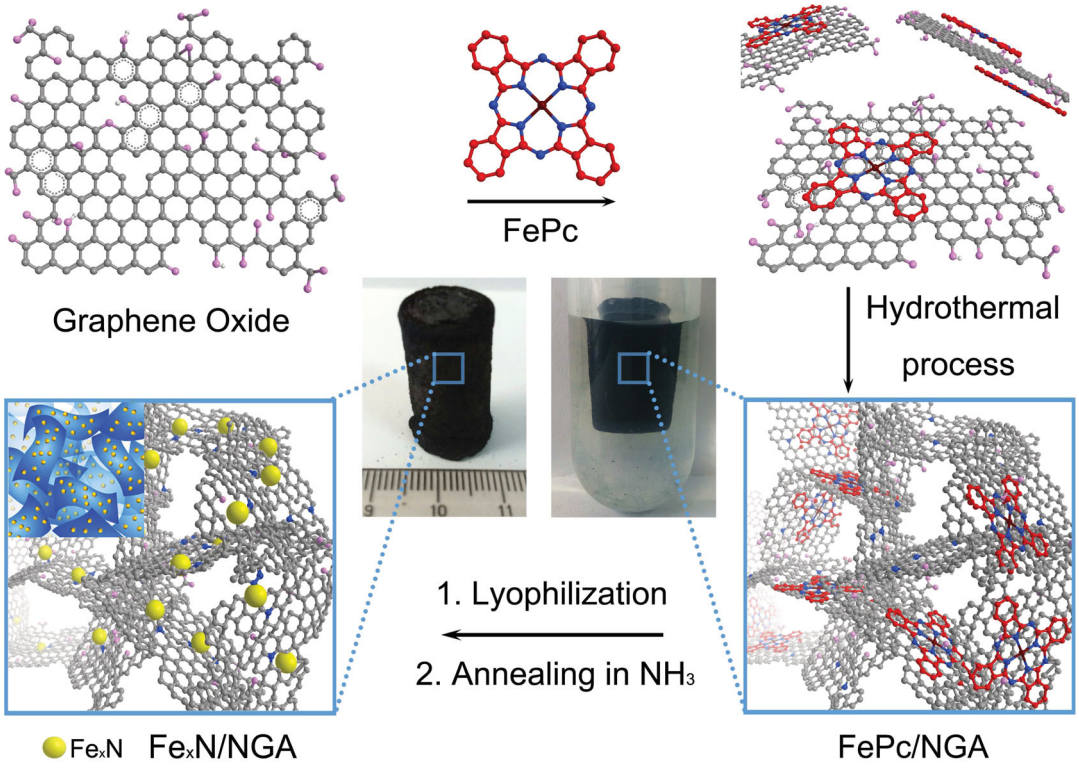

Scheme 1. Illustration of the preparation procedure of Fe_xN/NGA.

facilitate the formation of Fe–N–C sites because only atoms at the interface of the second phase and graphene are effective in forming such structures. Herein, we report 3D NG aerogel supported Fe_xN nanoparticles (Fe_xN/NGA) as an efficient synergistic ORR catalyst. The Fe_xN nanoparticles are mainly composed of the N-rich FeN phase and the particle size were controlled between 5 and 20 nm, which therefore significantly increased Fe–N–C density. The hybrid was prepared through a simple two-step method, namely hydrothermal assembly of graphene sheets followed by annealing in NH_3 atmosphere to enable the in situ growth of Fe_xN nanoparticles on graphene layers. The resulting Fe_xN/NGA was able to fully combine the advantages of both 3D graphene networks and iron nitride, achieving more positive onset potential and higher current density than the corresponding physical mixture of Fe_xN and NGA. Such synergistic effect suggested strong interactions between the two components. The catalytic activity of Fe_xN/NGA even outperformed that of commercial Pt/C at the same mass loading in alkaline solutions, together with superior durability and total resistance to methanol crossover. The strongly coupled hybrid meets the criteria of outstanding catalytic activity, excellent stability and low cost, and therefore has great potential to substitute Pt/C as an advanced electrocatalyst for ORR.

2. Results and Discussion

Fe_xN/NGA was synthesized via a two-step method which is schematically illustrated in **Scheme 1**. In the first step, GO and FePc with the same mass were mixed and sonicated in water to form a stable suspension (see Experimental Section for details). The dispersion was then transferred to a Teflon-lined autoclave and treated at 180 °C for 12 h to enable the assembly of GO sheets into a 3D aerogel and preliminary reduction of GO to reduced graphene oxide (rGO). During the hydrothermal process, FePc was encapsulated and anchored on rGO with the assistance of oxygen-containing functional groups on GO. The aerogel was lyophilized and annealed in NH_3 at 700 °C for 3 h to form strongly coupled Fe_xN/NGA hybrid.

Achieving the catalyst with maximized Fe–N–C density needs careful selection of the precursor. FePc had its unique advantages in the synthesis of Fe_xN/NGA. First of all, FePc has a conjugated structure, hence can attach to graphene through π–π interactions. Such interactions are crucial to prevent the restacking of GO during the hydrothermal process so as to form a porous structure and maintain a large surface area.[15] Second, FePc do not ionize in water and the π–π interactions allow FePc to form a stable suspension with GO without adding other stabilizer. Also, FePc serves as a source of Fe and N simultaneously. However, Fe precursors like $Fe(acac)_3$ needs other chemicals, such as PPy, to form a stable suspension.[8a] Therefore, using FePc as a precursor, the experimental procedure is simplified. Furthermore, due to the π–π interactions between FePc and graphene, FePc can be anchored on graphene which prevents the agglomeration of Fe_xN during pyrolysis process. As a result, small-sized particles are obtained. Finally, the majority of FePc phase remained unchanged after the hydrothermal process, which was essential for the formation of the N-rich phase FeN during pyrolysis in NH_3 as discussed below.

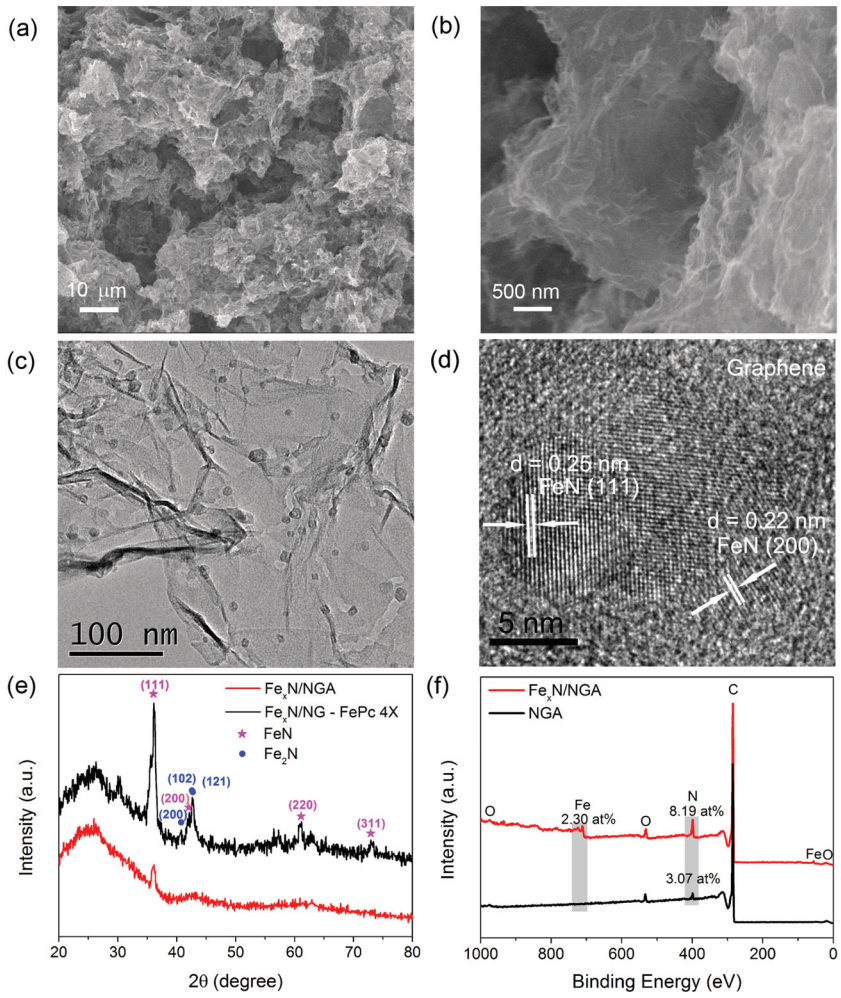

Figure 1. a,b) Typical SEM images of Fe_xN/NGA revealing a 3D macroporous structure. c) TEM and d) High-resolution TEM image of Fe_xN/NGA showing FeN nanoparticles on NG layer. e) XRD patterns of Fe_xN/NGA and Fe_xN/NG with excessive Fe source. The magenta and blue Miller indices correspond to FeN and Fe_2N, respectively. f) XPS spectra of Fe_xN/NGA and NGA.

The 3D structure of Fe_xN/NGA was first confirmed by scanning electron microscopy (SEM). The interconnected graphene networks showed a porous structure with micro-sized macropores (**Figure 1**a,b) . Transmission electron microscopy (TEM) image revealed that the sizes of nanoparticles encapsulated in graphene sheets were uniformly distributed with a range of 5 nm to 20 nm (Figure 1c). The small particle sizes could be attributed to the confinement of graphene layers which suppressed the agglomeration of nanoparticles.[16] Such confinement also enhanced the contact between nanoparticles and graphene layers so as to improve the ORR activity and stability of the hybrid.[8a] High resolution TEM revealed that the lattice fringes of the nanoparticles were consistent with FeN structure (Figure 1d). Two characteristic interplanar distances of the nanoparticles, 0.25 nm and 0.22 nm, correspond to (111) and (200) planes of FeN, respectively. X-ray diffraction (XRD) patterns of Fe_xN/NGA exhibited an extended peak at 26° corresponding to graphene, and a small peak at 36° corresponding to the (111) face of zinc blende FeN possibly because of the small particle size and relatively low loading of Fe_xN in the hybrid (Figure 1e). In order to better reveal the phases of the hybrid, we increased the FePc/GO weight ratio to 4 and followed the same preparation process of Fe_xN/NGA. XRD pattern of the product clearly demonstrated the existence of FeN and Fe_2N, and the intensity of FeN was significantly higher than that of Fe_2N, suggesting that the nanoparticles in Fe_xN/NGA were dominantly composed of FeN. We propose that FeN might derive from the decomposition of FePc at high temperature because FePc is a N-rich phase. Nevertheless, a part of FePc served as a source of nitrogen during the hydrothermal process. When phthalocyanine cycle decomposed, the released Fe element would form Fe_2O_3 which conversed into Fe_2N rather than FeN after the annealing process under NH_3. To confirm it, we recorded the XRD pattern of the FePc+GO mixture after hydrothermal reaction (Figure S1, Supporting Information), which displayed diffraction peaks of FePc and a small proportion of Fe_2O_3. Next, we annealed pure FePc and Fe_2O_3 under NH_3 atmosphere at 700 °C for 3 h, respectively, and XRD patterns of the products are shown in Figure S2a (Supporting Information). Both FePc and Fe_2O_3 conversed to Fe_2N. However, if we anneal pure FePc under NH_3 at 670 °C for 1.5 h, the product was FeN (Figure S2b, Supporting Information). The outcome was in coincidence with our hypothesis. Moreover, the result also suggested that NG layers were effective in protecting FeN from decomposing, which further indicated strong interactions between Fe_xN nanoparticles and graphene substrate.

X-ray photoelectron spectroscopy (XPS) analysis was employed to characterize the content of different elements in the hybrid (Figure 1f). Nitrogen and iron content in Fe_xN/NGA was 8.19 at.% and 2.30 at.%, respectively, while nitrogen content in pure NGA was only 3.07 at%. Supposing all the nitrogen atoms incorporated in graphene lattices were from NH_3 and the particles were only composed of FeN, the maximum N content in Fe_xN/NGA should be 5.37 at%, much lower than 8.19 at%. The result indicated that the high nitrogen content in the hybrid was not purely the outcome of NH_3 thermal treatment and existence of Fe_xN, demonstrating that FePc was able to incorporate nitrogen into graphene lattices. To verify nitrogen states in the hybrid, XPS measurements were performed from 394 eV to 408 eV. The deconvoluted N 1s spectrum of Fe_xN/NGA (Figure S3a, Supporting Information) revealed five nitrogen states: pyridinic N, Fe–N, pyrrolic N, graphitic N, and oxidized N, which peaked at 398.7 eV, 399.2 eV, 400.3 eV, 401.10 eV, and 402.7 eV, respectively.[7a,17] However, there was no peak of Fe–N in pure NGA (Figure S3b, Supporting Information). Note that the Fe–N here does not belong to pure Fe–N bonds, but to Fe–N bonds

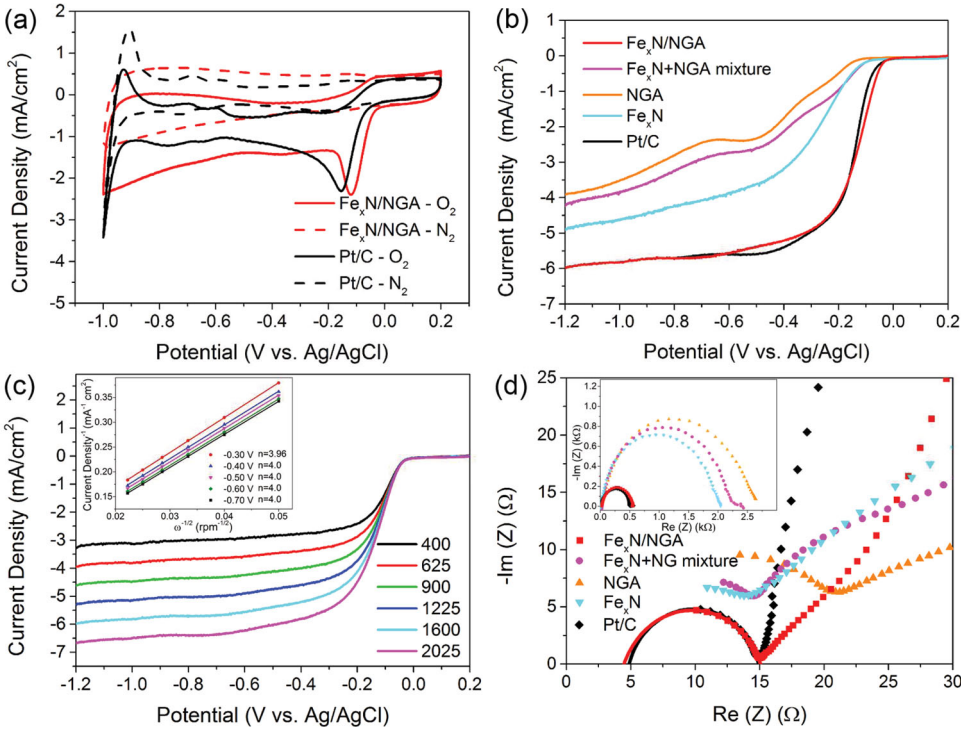

Figure 2. a) CV curves of Fe$_x$N/NGA hybrid and commercial Pt/C supported on glassy carbon electrodes in O_2-saturated (solid line) or N_2-saturated (dash line) 0.1 M KOH. b) RDE voltammograms of Fe$_x$N/NGA hybrid, Fe$_x$N+NGA mixture, NGA, free Fe$_x$N and Pt/C in O_2-saturated 0.1 M KOH at a sweep rate of 10 mV s^{-1} at 1600 rpm. Catalyst loading for all samples was 51 μg cm^{-2}. c) RDE voltammograms of Fe$_x$N/NGA hybrid in O_2-saturated 0.1 M KOH at various rotation speed at a scan rate of 10 mV s^{-1}. Inset in (c) shows Koutecky-Levich plots of Fe$_x$N/NGA hybrid at different potentials derived from RDE measurements. d) High-frequency region of the impedance spectra of Fe$_x$N/NGA, Fe$_x$N+NGA mixture, NGA, Fe$_x$N, and Pt/C at –0.1 V vs Ag/AgCl in 0.1 M KOH with an inset of the complete Nyquist plots.

in Fe–N–C structure. The binding energy of pure Fe–N bonds should be less than 398 eV since N could attract electrons from Fe.[18] However, N might donate its electrons to the conjugated graphene structure, resulting in the raise of binding energy to about 399.2 eV. The aerogel of GO and FePc after hydrothermal process was also characterized by XPS (Figure S4, Supporting Information). The O content in this product is 8.66 at.%, indicating that GO was significantly reduced during hydrothermal reaction because the original GO contains ≈32.3 at% oxygen according to our previous work.[2b] Together with the evidence that FePc was able to incorporate N into graphene, the main component of the aerogel after hydrothermal treatment was actually N-doped reduced GO. Furthermore, the O content in Fe$_x$N/NGA was only 3.88 at%, which demonstrate that thermal treatment in NH_3 further reduced N-doped reduced GO to NGA.

The electrocatalytic activity of Fe$_x$N/NGA was first evaluated by cyclic voltammetry (CV). The onset potential of the 3D hybrid was 0.01 V versus Ag/AgCl in O_2-saturated 0.1 M KOH solution, which was 20 mV more positive than that of commercial Pt/C (**Figure 2**a). The hybrid exhibited a remarkable oxygen reduction peak at –0.12 V in O_2-saturated KOH, whereas no cathodic peak for ORR was shown in N_2-saturated electrolyte, suggesting excellent ORR catalytic activity. Compared with Pt/C, both the peak potential and peak current density of Fe$_x$N/NGA were superior.

To further characterize the catalytic activity of Fe$_x$N/NGA hybrid, rotating disk electrode (RDE) measurement was applied. The onset potential of the hybrid was about 0.00 V versus Ag/AgCl (Figure 2b), close to that identified from CV measurement (0.01 V). The polarization curves of Fe$_x$N/NGA and Pt/C were similar, but under careful scrutiny, it was found that the hybrid owned a higher current density in the potential range from –0.02 V to –0.18 V and a more positive half-wave potential, indicating more active performance than Pt/C. The outstanding ORR catalytic activity was again confirmed by the much smaller Tafel slope of 52 mV per decade at low overpotentials compared with that of Pt/C (68 mV per decade) in 0.1 M KOH (Figure S5, Supporting Information). In comparison, NGA and free Fe$_x$N were also synthesized, but showed comparatively poor electrocatalytic activity with onset potentials at –0.09 V and –0.07 V, respectively, and significantly lower current densities than the hybrid. The physical mixture of the two above constituents failed to show any improvement, but compromised the performance of Fe$_x$N, suggesting that the remarkable catalytic activity of Fe$_x$N/NGA hybrid was facilitated by the strong interactions between Fe$_x$N nanoparticles and NGA.

The ORR mechanism occurred on the electrode was determined by RDE measurements at various rotation speed (Figure 2c), based on which the Koutecky-Levich (K-L) plots at different potentials were obtained. As shown in the inset of Figure 2c, the electron transfer number of the hybrid was able

to reach 4.0 at –0.4 V, indicating that Fe_xN/NGA hybrid catalyzed ORR mainly through a four electron pathway. The Tafel plot of Fe_xN/NGA showed a slope close to the Nernstian Tafel slope (59 mV) at low overpotentials (Figure S5, Supporting Information). In fact, many heat treated ORR catalysts based on transition metals possess similar Tafel slopes.[19] Such a slope indicated that the rate determining step of ORR might be the splitting of O–O bonds when two electrons transferred from active sites to adsorbed O_2 molecules and Fe(III) in Fe–N–C structure might be the sites for O_2 adsorption.[20]

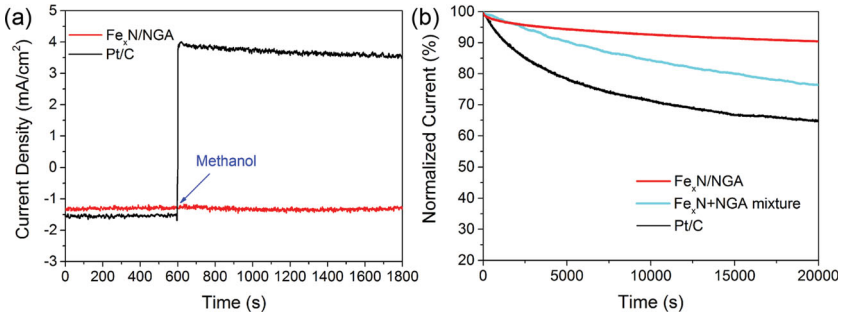

Figure 3. a) Chronoamperometric responses of Fe_xN/NGA and Pt/C at –0.25 V vs Ag/AgCl in O_2-saturated 0.1 M KOH followed by addition of 3 M methanol. b) Current-time responses of Fe_xN/NGA and Pt/C at –0.4 V vs Ag/AgCl in O_2-saturated 0.1 M KOH at 1600 rpm.

The electrochemical impedance spectroscopy (EIS) measurement at –0.1 V versus Ag/AgCl for various catalysts was conducted. It has been recognized that the high-frequency region of a Nyquist plot represents the charge transfer in catalyst layer while the low-frequency region is related to the mass transport processes.[21] Figure 2d showed the fitted semicircles of Fe_xN/NGA and Pt/C in high-frequency region with high-frequency intercepts equal to the electrolyte resistance and low-frequency intercepts equal to the sum of electrolyte resistance and charge transfer resistance. The electron transfer resistance of Fe_xN/NGA was only 10.5 Ω, similar to that of Pt/C (10.1 Ω). Such a low charge transfer resistance contributed to the excellent ORR catalytic performance of the hybrid. Moreover, the Fe_xN/NGA hybrid exhibited the smallest charge transfer resistance (Figure 2d) and mass transfer resistance (inset of Figure 2d) in comparison with either of its components or their physical mixture, demonstrating a strong coupling between Fe_xN and NGA, which significantly modified the electron structure of the graphene substrate, therefore improved the ORR catalytic activity.

For commercialization, apart from high catalytic activity, an ideal ORR catalyst should be able to afford the crossover of methanol from anode to cathode. The chronoamperometric responses of Fe_xN/NGA hybrid and Pt/C to the addition of 3 M methanol at –0.25 V versus Ag/AgCl were recorded in **Figure 3**a. Pt/C exhibited an appreciable current shift immediately after the injection of methanol, indicating the occurrence of methanol oxidation reaction, whereas no noticeable change was observed in the ORR current for the hybrid. The results demonstrated that Fe_xN/NGA hybrid possessed considerably better tolerance to methanol crossover than Pt/C.

Stability is another important aspect of fuel cell catalysts that needs considering. The chronoamperometric measurements of Fe_xN/NGA hybrid at a constant voltage of –0.4 V displayed only a ≈9% decrease of current density over 20 000 s, while the current of Pt/C decreased by ≈46% during the same operation (Figure 3b). It is worth noting that the current density of Fe_xN+NGA mixture was only ≈76% of its original value after 20 000 s, manifesting that free Fe_xN may not be stable when catalyzing ORR. However, when covalently supported and encapsulated by graphene layers, Fe_xN particles managed to remain stable over a long time. Such excellent durability was crucial for the future application of the hybrid.

We performed some other experiments to explore different conditions that may affect the electrochemical performance of Fe_xN/NGA. As seen in **Figure 4**a, the ORR catalytic activity of the hybrid of Fe_xN and NG sheets (Fe_xN/NGS) was significantly inferior to that of Fe_xN/NGA, displaying a more negative onset potential and lower current density. SEM image demonstrated that Fe_xN/NGS lacked a 3D interconnected porous structure (Figure S6a, Supporting Information), but its particle distribution and particle size displayed by TEM (Figure S6b, Supporting Information) were similar to that of Fe_xN/NGA. As a result, the performance distinction between Fe_xN/NGA and Fe_xN/NGS could be attributed to their disparate structures, that is, the relatively high surface area (116.9 m^2 g^{-1}) and large proportion of mesopores (ranged from 10 nm to 50 nm) in Fe_xN/NGA revealed by Brunauer-Emmett-Teller (BET) analysis (Figure S7a,b, Supporting Information) facilitated the diffusion of electrolyte and increased the contact between electrolyte and catalyst,[8a] whereas Fe_xN/NGS did not possess these features. BET measurements showed a surface area of only 7.1 m^2 g^{-1} and the pore size were mainly below 10 nm (Figure S8a,b, Supporting Information), which blocked the contact of oxygen, electrolyte and active sites.

We also investigated the performance of the hydrothermally assembled aerogels annealed under different atmospheres. The sample annealed under Ar displayed an onset potential which was 20 mV more negative than Fe_xN/NGA, and its current

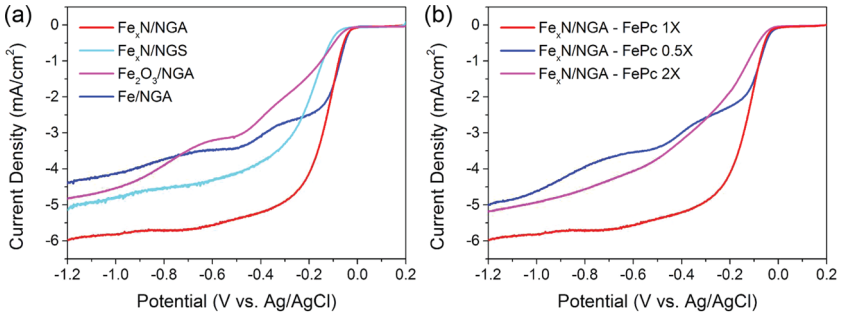

Figure 4. a) RDE measurements of Fe_xN/NGA, Fe_xN/NGS, Fe_2O_3/NGA, and Fe/NGA. b) RDE measurements of Fe_xN/NGA prepared with different amount of Fe source.

density was significantly lower as well (Figure 4a). XRD patterns exhibited that the second phase in the hybrid was mainly Fe_2O_3 rather than Fe_xN (Figure S9a, Supporting Information) (the product is termed as Fe_2O_3/NGA) and XPS measurement revealed only 5.5 at% N content, suggesting that the active sites were closely related to Fe_xN nanoparticles on graphene. When Fe atoms were surrounded by O atoms, Fe–N–C structures were unlikely to form, thus inhibited its ORR catalytic activity. The formation of Fe_2O_3 under inert atmosphere was the result of high oxygen content in the product after hydrothermal process. As shown in Figure S4 (Supporting Information), the O content in the aerogel after hydrothermal reaction was 8.66 at%, much higher than that in Fe_xN/NGA (3.88 at%). Unlike NH_3, Ar could not reduce oxygen-containing groups, thus the remaining oxygen would contribute to the formation of Fe_2O_3. We also annealed the hydrothermally formed aerogel under Ar/H_2 (5%) forming gas to produce Fe/NGA, as demonstrated by XRD analysis (Figure S9b, Supporting Information). Fe/NGA showed improved catalytic activity than Fe_2O_3/NGA, but it still catalyzed ORR through a two-step mechanism as manifested by the RDE curve from 0.00 V to 0.32 V and from 0.35 V to 0.62 V. Without the impediment of O atoms, Fe might form more Fe–N–C structures with NGA than Fe_2O_3, and that was probably the reason why it exhibited similar catalytic performance to Fe_xN/NGA at low overpotentials. However, Fe had to rely on relatively sparse N atoms on graphene surface to form Fe–N–C active sites, while Fe_xN nanoparticles, with N on their surfaces, were more effective to form such active sites on graphene. This distinction resulted in the disparate catalytic behaviors at high overpotentials.

To further explore how Fe_xN influenced the formation of active sites, we prepared Fe_xN/NGA with various Fe content. RDE measurements of these hybrids showed that the optimum weight ratio of GO and FePc was 1:1 to achieve the best onset potential and current density (Figure 4b). If we reduced the amount of FePc by half, the RDE curve exhibited an apparent two-step reduction process, corresponding to that from 0.00 V to –0.34 V and from –0.35 V to –0.71 V. This result corroborated that Fe_xN was closely related to the active sites on graphene. Insufficient Fe_xN led to fewer active sites and, as a result, the two-step reduction of oxygen. However, if we double the quantity of FePc, the current density was compromised, although the onset potential remained the same as Fe_xN/NGA with 1X FePc precursor. The performance degradation when overloading Fe_xN could be attributed to the much larger Fe_xN nanoparticles (up to ≈100 nm) (Figure S10, Supporting Information) on graphene which might block the pores in graphene support[22] and the uncoordinated Fe_xN particles which increased the charge transfer resistance between catalyst and electrolyte. In addition, as shown in **Table 1**, XPS analysis revealed that the Fe and N content raised proportional to the increasing amount of FePc. O content remained stable when FePc increased from 0.5X to 1X, while it raised evidently when the amount of FePc changed from 1X to 2X, suggesting possible formation of Fe–O bonds which affected the density of Fe–N–C active sites. Further amplifying the amount of FePc resulted in failure to form aerogels.

To achieve catalysts with more positive onset potential and lower charge transfer resistance, it is crucial to figure out their influencing factors. The onset potentials of Fe_xN/NGA, Fe_2O_3/NGA, and Fe/NGA were similar, suggesting that they were not determined by the density of Fe–N–C active sites. However, the onset potential of Fe_xN/NGS was more negative. Therefore, onset potential could be related to surface area and pore size. On the other hand, Fe_xN/NGA, Fe/NGA, and Fe_xN/NGA with 0.5X FePc all exhibited almost the same current densities at very low overpotentials, representing comparable charge transfer rate. EIS measurement further confirmed this result, as can be seen in Figure S11 (Supporting Information). These three materials showed semicircles with similar size in high-frequency region. Therefore, charge transfer rate is not affected by the density of active sites when overpotential is low, but higher active sites lead to faster charge transfer at high overpotentials. Considering that the surface of electrode is saturated with O_2, this phenomenon may be explained as that Fe–N–C sites in these catalysts were in excess at low overpotentials. In other words, a part of active sites could adsorb but could not reduce O_2. When the density of Fe–N–C active sites are low, as in the case of Fe_2O_3/NGA, the charge transfer rate was considerably reduced. Fe_xN/NGA with 2X FePc showed higher charge transfer resistance due to the obstruction of transfer passages by large particles. Their increased charge transfer resistance were again demonstrated by the larger semicircles compared with Fe_xN/NGA in Nyquist plot (Figure S11, Supporting Information). The results described above demonstrate that higher Fe–N–C densities and smaller particle size were two factors capable of facilitating charge transfer.

Table 1. Content of Fe, N, and O in samples with different amount of Fe source.

Sample	Fe [at%]	N [at%]	O [at%]
Fe_xN/NGA-FePc 0.5X	1.32	6.85	3.74
Fe_xN/NGA-FePc 1X	2.30	8.19	3.88
Fe_xN/NGA-FePc 2X	4.34	9.45	5.25

3. Conclusions

In summary, we synthesized a novel 3D Fe_xN/NGA hybrid via a facile two-step method. FeN, the dominant phase of Fe_xN in the hybrid, were more effective in forming Fe–N–C active sites with NGA. In addition, the Fe_xN nanoparticles sized mainly from 5 nm to 20 nm. Such small sizes allowed the formation of more active sites on their surfaces. Due to the rich Fe–N–C structures together with the 3D macroporous morphology with high surface area, the Fe_xN/NGA hybrid demonstrated greatly enhanced synergistic catalytic activity towards ORR in alkaline solution compared with the physical mixture of its two components. At the same mass loading, the Fe_xN/NGA hybrid outperformed Pt/C in terms of onset potential, current density at potential greater than –0.18 V versus Ag/AgCl, resistance to methanol crossover, and stability. In general, we discovered that surface area, porosity, density of Fe–N–C active sites, and size of particles on graphene were able to affect the catalysts' ORR activity considerably. The outstanding catalytic performance and low

cost of Fe_xN/NGA hybrid make it a promising candidate to replace Pt in fuel cells and our synthetic strategy may promote the emergence of more 3D graphene based nanocomposites for energy related applications.

4. Experimental Section

Synthesis of Graphene Oxide (GO): GO was prepared from natural graphite powder by a modified Hummer's method.[23] Graphite powder (1 g), $NaNO_3$ (0.5 g), and 23 mL of concentrated sulfuric acid were added into a 250 mL round-bottom flask and stirred at room temperature for 24 h. Next, the flask was moved into an ice bath and 3 g $KMnO_4$ was slowly added under vigorous agitation. The flask was then heated in a water bath at 38 °C for 2 h. 46 mL of water was gradually added to the flask and the suspension was allowed to stir for 15 min. The suspension was diluted by 140 mL of water and the reaction was ended by addition of 10 mL of 30% H_2O_2. 10 min later, the bright yellow suspension was centrifuged and washed with 10% HCl solution twice. The precipitate was finally washed with water, collected by centrifugation and dried in a vacuum oven at 70 °C overnight.

Synthesis of Fe_xN/NGA Hybrid, Fe_xN/NGS Hybrid, NGA, and Fe_xN: In a typical process, 60 mg GO and 60 mg iron (II) phthalocyanine (FePc) were dispersed in 10 mL of water and sonicated for 1 h to form a stable suspension. It was then transferred to a 50 mL Teflon-lined autoclave, followed by addition of 30 mL of water, and hydrothermally treated at 180 °C for 12 h. The as-synthesized aerogel was lyophilized and annealed in NH_3 atmosphere at 700 °C for 3 h.

Fe_xN/NGS was prepared by the same method as Fe_xN/NGA hybrid, except that only 20 mg GO and 20 mg FePc were involved in the hydrothermal treatment. For the preparation of NGA, no FePc was added during the hydrothermal procedure. In the case of free Fe_xN, no GO was added and the product after hydrothermal treatment was annealed in NH_3 at 670 °C for 1.5 h.

Structure and Morphology Characterizations: SEM, TEM and HRTEM images were recorded on a Hitachi S4800, FEI Tecnai T20 and FEI Tecnai F30, respectively. XRD patterns were acquired on a Philips X'Pert Pro diffractometer with Cu Kα ($\lambda = 1.5405$ Å) radiation. XPS measurements were carried out on an Axis Ultra (Kratos Analytical Ltd.) imaging photoelectron spectrometer and the C 1s peak at 284.8 eV was taken as an internal standard.

Electrochemical Measurements: Electrochemical characterizations were performed on a CHI760C electrochemical workstation with a three-electrode system. A glassy carbon electrode of 5 mm in diameter was used as the working electrode, a Pt foil as the counter electrode and a saturated Ag/AgCl electrode as the reference electrode. For electrode preparation, 2 mg sample catalyst was first homogeneously dispersed in ethanol to form a 1 mg mL^{-1} suspension by sonication for at least 30 min. Next, 10 μL of the catalyst ink was loaded onto the glassy carbon electrode, followed by dropping of 2 μL of Nafion (0.1 wt%) solution. Commercial Pt/C (20 wt% Pt on Vulcan XC-72) electrode was prepared by the same procedure. Catalyst loading for all samples, including Pt/C, was 50 μg cm^{-2}.

0.1 M KOH was saturated with O_2 by bubbling oxygen for 20 min before testing. For cyclic voltammetry (CV) measurements, the working electrode was cycled between –1.2 V and 0.2 V at a scan rate of 100 mV s^{-1} with continuous O_2 flow. For control experiments in N_2 saturated KOH, switching O_2 to N_2 and other procedures remain unchanged. Rotating disk electrode (RDE) measurements were conducted at different rotating speed from 400 to 2025 rpm at a scan rate of 10 mV s^{-1}. Electrochemical impedance spectroscopy was measured in 0.1 M KOH at –0.1 V. The frequency is from 10^{-3} to 10^5 Hz and the potential amplitude is 5 mV.

Koutecky-Levich (K-L) plots were analyzed at various potentials to determine the number of electrons transferred based on K-L equation:[24]

$$\frac{1}{J} = \frac{1}{J_K} + \frac{1}{J_L} = \frac{1}{J_K} + \frac{1}{B\omega^{1/2}} \quad (1)$$

$$B = 0.2nF\left(D_{O_2}\right)^{2/3} \nu^{-1/6} C_{O_2} \quad (2)$$

Where J and J_K are the measured and kinetic-limiting current densities, ω is the rotation speed, n is transferred electron number, F is the Faraday constant (F = 96485 C mol^{-1}), D_{O_2} is the diffusion coefficient of O_2 ($D_{O_2} = 1.9 \times 10^{-5}$ cm^2 s^{-1}), ν is the kinematic viscosity (ν = 0.01 cm^2 s^{-1}), and C_{O_2} is the concentration of O_2 in the solution ($C_{O_2} = 1.2 \times 10^{-6}$ mol cm^{-3}). The constant 0.2 is adopted when rotation speed is expressed in rpm. For Tafel plots, the kinetic current was determined after mass-transport correction of RDE curves by

$$J_K = \frac{J \times J_L}{J_L - J} \quad (3)$$

Supporting Information

Supporting Information is available from the Wiley Online Library or from the author.

Acknowledgements

This work was supported in part by the NSFC (51125001, 51172005, 90922033), the National Basic Research Program of China (2010CB934601), the Doctoral Program (20120001110078) and New Century Talent of the Education Ministry of China (NCET-09–0177), the Natural Science Foundation of Beijing (2122022), Aeronautic Science Fund (2010ZF71003) and Yok Ying Tung Fund (122043).

Received: November 19, 2013
Revised: December 12, 2013
Published online: February 3, 2014

[1] a) Y. Li, W. Zhou, H. Wang, L. Xie, Y. Liang, F. Wei, J.-C. Idrobo, S. J. Pennycook, H. Dai, *Nat. Nanotechnol.* **2012**, *7*, 394; b) S. Chen, J. Bi, Y. Zhao, L. Yang, C. Zhang, Y. Ma, Q. Wu, X. Wang, Z. Hu, *Adv. Mater.* **2012**, *24*, 5593; c) Y. Tang, B. L. Allen, D. R. Kauffman, A. Star, *J. Am. Chem. Soc.* **2009**, *131*, 13200; d) C. H. Choi, S. H. Park, S. I. Woo, *ACS Nano* **2012**, *6*, 7084; e) W. Xiong, F. Du, Y. Liu, A. Perez, M. Supp, T. S. Ramakrishnan, L. Dai, L. Jiang, *J. Am. Chem. Soc.* **2010**, *132*, 15839; f) F. Gao, G.-L. Zhao, S. Yang, J. J. Spivey, *J. Am. Chem. Soc.* **2012**, *135*, 3315.

[2] a) X. Cui, C. Zhang, R. Hao, Y. Hou, *Nanoscale* **2011**, *3*, 2118; b) C. Zhang, R. Hao, H. Liao, Y. Hou, *Nano Energy* **2013**, *2*, 88; c) Y. Zheng, Y. Jiao, L. Ge, M. Jaroniec, S. Z. Qiao, *Angew. Chem. Int. Ed.* **2013**, *52*, 3110; d) L. Qu, Y. Liu, J.-B. Baek, L. Dai, *ACS Nano* **2010**, *4*, 1321; e) Z.-H. Sheng, L. Shao, J.-J. Chen, W.-J. Bao, F.-B. Wang, X.-H. Xia, *ACS Nano* **2011**, *5*, 4350; f) J. Liang, Y. Jiao, M. Jaroniec, S. Z. Qiao, *Angew. Chem. Int. Ed.* **2012**, *51*, 11496.

[3] a) D. S. Su, G. Sun, *Angew. Chem. Int. Ed.* **2011**, *50*, 11570; b) S. N. S. Goubert-Renaudin, A. Wieckowski, *J. Electroanal. Chem.* **2011**, *652*, 44; c) K. Kamiya, K. Hashimoto, S. Nakanishi, *Chem. Commun.* **2012**, *48*, 10213.

[4] a) Y. Liang, Y. Li, H. Wang, J. Zhou, J. Wang, T. Regier, H. Dai, *Nat. Mater.* **2011**, *10*, 780; b) Y. Liang, H. Wang, J. Zhou, Y. Li, J. Wang, T. Regier, H. Dai, *J. Am. Chem. Soc.* **2012**, *134*, 3517; c) Y. Liang, H. Wang, P. Diao, W. Chang, G. Hong, Y. Li, M. Gong, L. Xie, J. Zhou, J. Wang, T. Z. Regier, F. Wei, H. Dai, *J. Am. Chem. Soc.* **2012**, *134*, 15849; d) Y. Tan, C. Xu, G. Chen, X. Fang, N. Zheng, Q. Xie, *Adv. Funct. Mater.* **2012**, *22*, 4584.

[5] a) N. Mahmood, C. Zhang, J. Jiang, F. Liu, Y. Hou, *Chem. Eur. J.* **2013**, *19*, 5183; b) H. Wang, Y. Liang, Y. Li, H. Dai, *Angew. Chem. Int. Ed.* **2011**, *50*, 10969; c) Z.-Y. Shih, A. P. Periasamy, P.-C. Hsu, H.-T. Chang, *Appl. Catal. B* **2013**, *132–133*, 363.

[6] a) C. Zhang, R. Hao, H. Yin, F. Liu, Y. Hou, *Nanoscale* **2012**, *4*, 7326; b) H. Tang, H. Yin, J. Wang, N. Yang, D. Wang, Z. Tang, *Angew. Chem. Int. Ed.* **2013**, *52*, 5585; c) D. Pan, M. Ombaba, Z.-Y. Zhou, Y. Liu, S. Chen, J. Lu, *ACS Nano* **2012**, *6*, 10720; d) R. Cao, R. Thapa, H. Kim, X. Xu, M. Gyu Kim, Q. Li, N. Park, M. Liu, J. Cho, *Nat. Commun.* **2013**, *4*, 2076; e) Y. Jiang, Y. Lu, X. Lv, D. Han, Q. Zhang, L. Niu, W. Chen, *ACS Catal.* **2013**, *3*, 1263.

[7] a) H. Peng, Z. Mo, S. Liao, H. Liang, L. Yang, F. Luo, H. Song, Y. Zhong, B. Zhang, *Sci. Rep.* **2013**, *3*, 1765; b) S. Zhang, H. Zhang, Q. Liu, S. Chen, *J. Mater. Chem. A* **2013**, *1*, 3302; c) H. T. Chung, J. H. Won, P. Zelenay, *Nat. Commun.* **2013**, *4*, 1922.

[8] a) Z. S. Wu, S. Yang, Y. Sun, K. Parvez, X. Feng, K. Mullen, *J. Am. Chem. Soc.* **2012**, *134*, 9082; b) Y.-C. Yong, X.-C. Dong, M. B. Chan-Park, H. Song, P. Chen, *ACS Nano* **2012**, *6*, 2394; c) K. Gong, F. Du, Z. Xia, M. Durstock, L. Dai, *Science* **2009**, *323*, 760; d) J.-S. Lee, G. S. Park, S. T. Kim, M. Liu, J. Cho, *Angew. Chem. Int. Ed.* **2013**, *52*, 1026.

[9] S. Guo, S. Dong, *Chem. Soc. Rev.* **2011**, *40*, 2644.

[10] a) Y. Xue, D. Yu, L. Dai, R. Wang, D. Li, A. K. Roy, F. Lu, H. Chen, Y. Liu, J. Qu, *Phys. Chem. Chem. Phys.* **2013**; b) Z. Lin, G. H. Waller, Y. Liu, M. Liu, C. Wong, *Nano Energy* **2013**, *2*, 241.

[11] G. Wu, K. L. More, C. M. Johnston, P. Zelenay, *Science* **2011**, *332*, 443.

[12] K. Parvez, S. Yang, Y. Hernandez, A. Winter, A. Turchanin, X. Feng, K. Müllen, *ACS Nano* **2012**, *6*, 9541.

[13] L. Wang, J. Yin, L. Zhao, C. Tian, P. Yu, J. Wang, H. Fu, *Chem. Commun.* **2013**, *49*, 3022.

[14] a) U. I. Kramm, I. Herrmann-Geppert, P. Bogdanoff, S. Fiechter, *J. Phys. Chem. C* **2011**, *115*, 23417; b) H. Meng, N. Larouche, M. Lefèvre, F. Jaouen, B. Stansfield, J.-P. Dodelet, *Electrochim. Acta* **2010**, *55*, 6450.

[15] Y. Zhao, C. Hu, Y. Hu, H. Cheng, G. Shi, L. Qu, *Angew. Chem. Int. Ed.* **2012**, *51*, 11371.

[16] a) S. Yang, X. Feng, S. Ivanovici, K. Müllen, *Angew. Chem. Int. Ed.* **2010**, *49*, 8408; b) D. Chen, G. Ji, Y. Ma, J. Y. Lee, J. Lu, *ACS Appl. Mater. Interfaces* **2011**, *3*, 3078.

[17] a) G. Wu, C. M. Johnston, N. H. Mack, K. Artyushkova, M. Ferrandon, M. Nelson, J. S. Lezama-Pacheco, S. D. Conradson, K. L. More, D. J. Myers, P. Zelenay, *J. Mater. Chem.* **2011**, *21*, 11392; b) C. Zhang, L. Fu, N. Liu, M. Liu, Y. Wang, Z. Liu, *Adv. Mater.* **2011**, *23*, 1020; c) L. Lai, J. R. Potts, D. Zhan, L. Wang, C. K. Poh, C. Tang, H. Gong, Z. Shen, J. Lin, R. S. Ruoff, *Energy Environ. Sci.* **2012**, *5*, 7936; d) T. Hung, M. Tu, C. Tsai, C. Chen, R. Liu, W. Liu, M. Lo, *Int. J. Hydrogen Energy* **2013**, *38*, 3956.

[18] X. Wang, W. T. Zheng, H. W. Tian, S. S. Yu, W. Xu, S. H. Meng, X. D. He, J. C. Han, C. Q. Sun, B. K. Tay, *Appl. Surf. Sci.* **2003**, *220*, 30.

[19] a) H. Schulenburg, S. Stankov, V. Schünemann, J. Radnik, I. Dorbandt, S. Fiechter, P. Bogdanoff, H. Tributsch, *J. Phys. Chem. B* **2003**, *107*, 9034; b) E. HaoYu, S. Cheng, K. Scott, B. Logan, *J. Power Sources* **2007**, *171*, 275; c) M. Lefevre, E. Proietti, F. Jaouen, J. P. Dodelet, *Science* **2009**, *324*, 71.

[20] J. Chlistunoff, *J. Phys. Chem. C* **2011**, *115*, 6496.

[21] P. M. Gomadam, J. W. Weidner, *Int. J. Energy Res.* **2005**, *29*, 1133.

[22] G. Q. Sun, J. T. Wang, S. Gupta, R. F. Savinell, *J. Appl. Electrochem.* **2001**, *31*, 1025.

[23] W. S. Hummers, R. E. Offeman, *J. Am. Chem. Soc.* **1958**, *80*, 1339.

[24] G. Sohn, H. Choi, I. Jeon, D. W. Chang, L. Dai, J. Baek, *ACS Nano* **2012**, *6*, 6345.